crystals

MDPI

*Review*

# B-Site Cation Ordering in Films, Superlattices, and Layer-by-Layer-Grown Double Perovskites

**Philipp Ksoll [1,*], Christoph Meyer [1], Leonard Schüler [1], Vladimir Roddatis [2] and Vasily Moshnyaga [1]**

[1] Erstes Physikalisches Institut, Georg-August-Universität Göttingen, Friedrich-Hund-Platz 1, 37077 Göttingen, Germany; christoph.meyer@phys.uni-goettingen.de (C.M.); leonard.schueler@stud.uni-goettingen.de (L.S.); vmosnea@gwdg.de (V.M.)

[2] GFZ German Research Centre for Geosciences, Helmholtz Centre Potsdam, Telegrafenberg, 14473 Potsdam, Germany; vladimir.roddatis@gfz-potsdam.de

* Correspondence: pksoll@gwdg.de

**Abstract:** The preparation of cation-ordered thin films of correlated oxides is of great interest for both fundamental and applied research. The scientific long-term vision is strongly motivated by the perspective of studying electronic correlations in condensed matter without the presence of chemical or quenched disorder. A promising material platform provides double perovskite $A_2BB'O_6$ bulk samples with different types of B/B′ ordering. However, the growth of A- and/or B-site-ordered correlated oxide thin films is known to be a challenging task. In this review, we evaluate the growth of double perovskite $A_2BB'O_6$ thin films by means of well-elaborated physical vacuum deposition techniques, such as pulsed laser deposition (PLD) and sputtering and compare them with a close-to-equilibrium growth with the metalorganic aerosol deposition (MAD) technique. The latter was further developed to grow an emergent interfacial double perovskite phase in $LaNiO_3/LaMnO_3$ superlattices, and finally, by way of a layer-by-layer route. The growth of $La_2CoMnO_6$ films on $SrTiO_3(111)$ substrates by sequential deposition of single perovskite layers of $LaCoO_3/LaMnO_3/LaCoO_3/\ldots$ was demonstrated and the film properties were compared to those obtained within the state-of-the art growth mode.

**Keywords:** double perovskites; cation ordering; physical vacuum deposition; metalorganic aerosol deposition



**Citation:** Ksoll, P.; Meyer, C.; Schüler, L.; Roddatis, V.; Moshnyaga, V. B-Site Cation Ordering in Films, Superlattices, and Layer-by-Layer-Grown Double Perovskites. *Crystals* **2021**, *11*, 734. https://doi.org/10.3390/cryst11070734

Academic Editor: Leonid Kustov

Received: 21 May 2021
Accepted: 23 June 2021
Published: 25 June 2021



## 1. Introduction

Electronic correlations together with a complex interplay between charge, spin, and lattice degrees of freedom in transition metal oxides with perovskite structure result in interesting physical phenomena and promising functional properties, such as colossal magnetoresistance (CMR) in mixed-valence manganites [1,2] and high-$T_C$ superconductivity in cuprates [3,4]. The possibility of controlling these intriguing phenomena and using them in potential device applications have motivated long-term research in perovskite oxides with the general formula $ABO_3$. The A and B positions can be occupied by rare earth (La, Pr, Nd, etc.) and transition metal (Mn, Co, Ni, etc.) cations, respectively, having different oxidation states (valences) and cation sizes. Moreover, the perovskite structure enables systematic chemical doping and substitution on both A- ($A_{1-x}A'_xBO_3$) and B-sites ($AB_xB'_{1-x}O_3$), with A′ as di-(Ca, Sr, Ba), tri-(La, Pr, Nd), or mono-valent (Li, Na) cations, and BB′ as transition metal cations, e.g., Ni, Mn, Co, etc. In addition to the random distribution of cations between the A- and B-positions, such as that occurring in an alloy, a cation ordering within the A- or B-sites or even a simultaneous ordering within A- and B-sites in the perovskite structure can be achieved [5–9].

Cation ordering can play a crucial role in the above-mentioned interplay of charge, spin, and lattice degrees of freedoms, resulting in specific electrical and magnetic properties, which cannot be realized in a cation-disordered material. Particularly interesting are

the so-called double perovskites (DP) with the sum formula $A_2BB'O_6$, where B-sites are occupied in an ordered manner by two different cations with a B/B′ ratio of 1:1. The degree of the B-site ordering determines the crystal structure and magnetic exchange interactions between the respective magnetic B-cations. Generally, B-site ordering can be controlled by *steric* (cation sizes) and *Coulomb interactions* (oxidation states) between the chosen B/B′ cations [7,8], which can be considered intrinsic conditions. However, the realizations of B-site ordering are strongly influenced by the *growth conditions* of a DP material as well as by unavoidable one-dimensional (vacancies and impurities) and two-dimensional (interfaces and grain boundaries) *defects*. All these intrinsic and extrinsic material aspects, preventing an ideal 100% B-site ordering, nevertheless allow researchers to control the physical and physico-chemical properties of DP to a large extent. Striking examples of such a control provide: (a) the half-metallic double perovskite $Sr_2FeMoO_6$ [10], in which the spin polarization of electrons at the Fermi level as well as magnetism are drastically enhanced by the degree of B-site ordering, and (b) the dielectric $Pb_2ScTaO_6$, displaying a ferroelectric or relaxor dielectric behavior for the fully ordered or disordered Sc/Ta distribution, respectively [11]. Great interest in the potential applications of DPs is motivated by observations of pronounced magnetodielectric effects [12–14], photo- and electro-catalysis [15], as well as by very recent photovoltaic studies [15–17].

Our motivation to write this short review is based on the conviction that the further development of new routes and techniques for the growth of cation-ordered correlated oxide films could produce an essential breakthrough in both fundamental and applied research. Indeed, the study of correlation effects in condensed matter without chemical disorder could particularly impact the areas of classical and quantum phase transitions, low-dimensional systems, and nanoscale physics. Potential applications would strongly benefit from the development of advanced growth routes that could controllably and reproducibly establish a high degree of cation ordering by the fine tuning of processing conditions at the atomic scale.

This review article is organized in such a way that we begin (part 2) with a short discussion of the general aspects and models of cation ordering in bulk DPs. In the third part, we address the B-site ordering and its quantification and manifestations in thin films, prepared by different physical vapor deposition (PVD) techniques such as pulsed laser deposition (PLD), sputtering, molecular beam epitaxy (MBE), and chemical routes such as metalorganic aerosol deposition (MAD) and polymer-assisted deposition (PAD). At this point, the discussion is focused on the influence of specific growth conditions inherent to different deposition techniques as well as on the epitaxial strain actuated by the different single crystalline substrates. We have mainly limited ourselves to the $La_2CoMnO_6$ (LCMO) and $La_2NiMnO_6$ (LNMO) films as the most studied magnetic DP materials. Finally, the recent results on the realization of B-site ordering at interfaces in perovskite superlattices, as well as the application of the layer-by-layer growth, will be presented and discussed.

## 2. General Aspects of B-Site Cation Ordering in Bulk Double Perovskites

If the different B cations are randomly distributed in the crystal, the DP material is considered to be disordered and the notation $AB_{0.5}B'_{0.5}O_3$ is used, while for alternatively occupied B-sites, DP is viewed to be ordered and the notation is $A_2BB'O_6$. The B-site arrangements of the ordered $A_2BB'O_6$ DP (visualized by the "Vesta" program [18]), can be set in three ways [7,8], as shown in Figure 1a the NaCl type of ordering with B and B′ occupations alternating in all three spatial directions; Figure 1b the columnar order with alternating B/B′ occupations in two spatial directions; and Figure 1c the B/B′ layered type of ordering, with alternating planes occupied by B and B′ cations. Since in most cases the B and B′ cations possess different valences or oxidation states in the ordered case, the NaCl type of ordering is energetically favorable from the electrostatic point of view, as B and B′ cations are spatially separated from each other [7,8]. This is the reason why the NaCl type of ordering is the most observed type of B-site ordering.

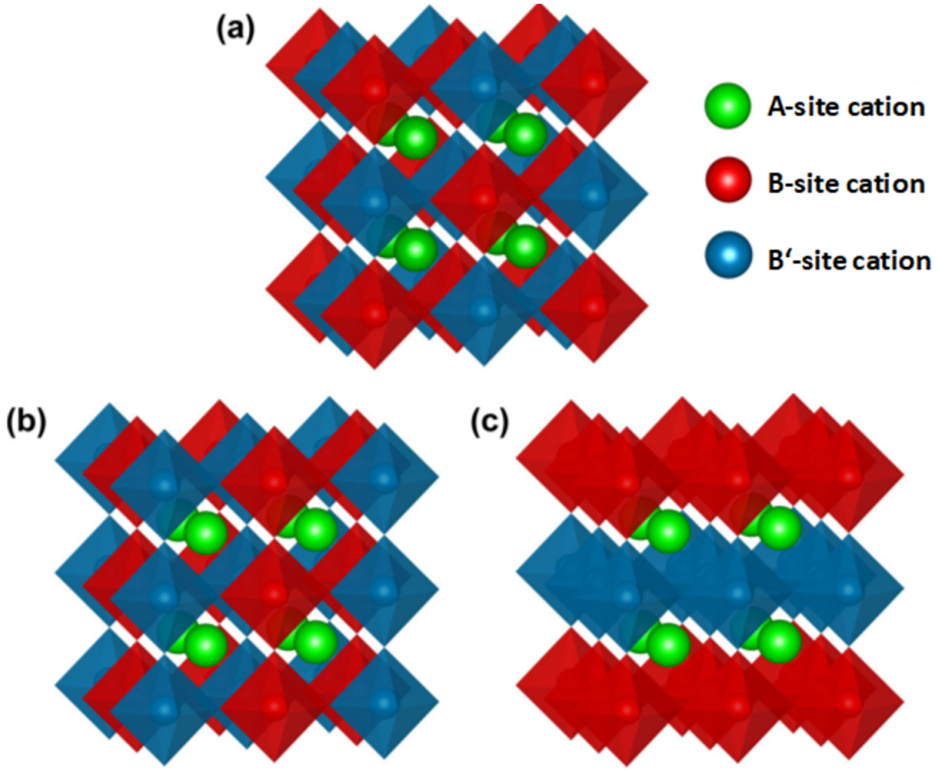


**Figure 1.** Three different types of the B-site ordering: (**a**) NaCl type; (**b**) columnar; and (**c**) layered, redrawn with the program Vesta (ref. [18]).

Similar to a simple perovskite oxide $ABO_3$, the crystal structure of the B-site ordered DP is influenced by A- and B-site cation radii, as described by the tolerance factor $t = (r_A + r_O)/\sqrt{2}(r_B + r_O)$ and the $BO_6$ octahedral tilt [8,19,20]. In the ideal case of fully matched A- and B-cations, t = 1 and the undistorted *Fm3m* cubic structure would be realized. In the most practically relevant cases, the tolerance factors are smaller (t < 1) and the crystal symmetry is reduced to the tetragonal *I4/m* or monoclinic $P2_1/n$ space group. In contrast, the disordered DPs often crystallize in an orthorhombic *Pbnm* structure [5,8,21–25]. Assuming an ideal NaCl arrangement of B/B′ cations (t = 1), an enlarged unit cell (u.c.) composed of two cubic perovskite u.c. with B and B′ cations in each one, can be considered $a_{DP} = 2a_p$ and given the name "double perovskite". This issue becomes particularly clear when considering crystallographic planes with only the same cations, i.e., planes with B- or B′-cations, oriented perpendicularly to the [111]-axis within the NaCl structure of ordering (see Figure 2). One can view this as a crystal superstructure, composed of the $ABO_3$ and $AB'O_3$ perovskite atomic layers, [8,26] which appears due to the doubling of the unit cell in the ordered DP along the [111] direction. Such a superstructure could be resolved in X-ray diffraction (XRD) measurements as an additional superstructure peak (1/2 1/2 1/2), which can be assigned to the doubled u.c. of the ordered DP.

As already mentioned, the physical properties are strongly influenced by the degree of B-site ordering, which as well depends on various driving forces during crystal growth. Considering the NaCl type of ordering, the electrostatics, and thus the difference in valences of the B cations $\Delta Z_B = |Z_B - Z_{B'}|$, play an important role. Specifically, the larger the B/B′ valence mismatch, the higher the degree of order since this maximizes the distance between the B and B′ cations viewed as effective ionic charges $Z_B$ and $Z_{B'}$. Empirical studies show that DPs with a valence difference of $\Delta Z_B > 2$ are usually ordered, and those with a difference of $\Delta Z_B < 2$ are disordered. For $\Delta Z_B = 2$, both ordered and disordered cases are possible [7,8]. The second driving factor of B-site ordering is the cation size (radii) mismatch $\Delta R_B = |R_B - R_{B'}|$: the larger the $\Delta R_B$, the larger the local lattice strain, which thus drives B-site ordering. Interestingly, for an LCMO DP with $Co^{2+}$ and $Mn^{4+}$ cations

in the fully ordered state, the valence and site mismatches are coupled with each other in $\Delta R = |R_{Co2+} - R_{Mn4+}| = 21$ pm, which is considerably larger than the size mismatch between $Co^{3+}$ and $Mn^{3+}$ cations in $\Delta R = |R_{Co3+} - R_{Mn3+}| = 3$ pm. A similar issue can be observed in the Ni/Mn ordering as $\Delta R = |R_{Ni2+} - R_{Mn4+}| = 16$ pm >> $\Delta R = |R_{Ni3+} - R_{Mn3+}| = 4$ pm. The values of cation radii were taken from ref. [27]. From the energetic point of view, the gain in the potential electrostatic (Coulomb) energy will be obtained when both $Co^{2+}$ and $Mn^{4+}$ are separated from each other. But this has to be compensated by the increased elastic energy of the lattice due to local strains as the size mismatch between cations in the ordered phase ($Co^{2+}$ and $Mn^{4+}$) is much larger than the size mismatch in a fully disordered state ($Co^{3+}$ and $Mn^{3+}$). It looks probable that the NaCl type of ordering is favorable for the compensation of both charge and size mismatches.

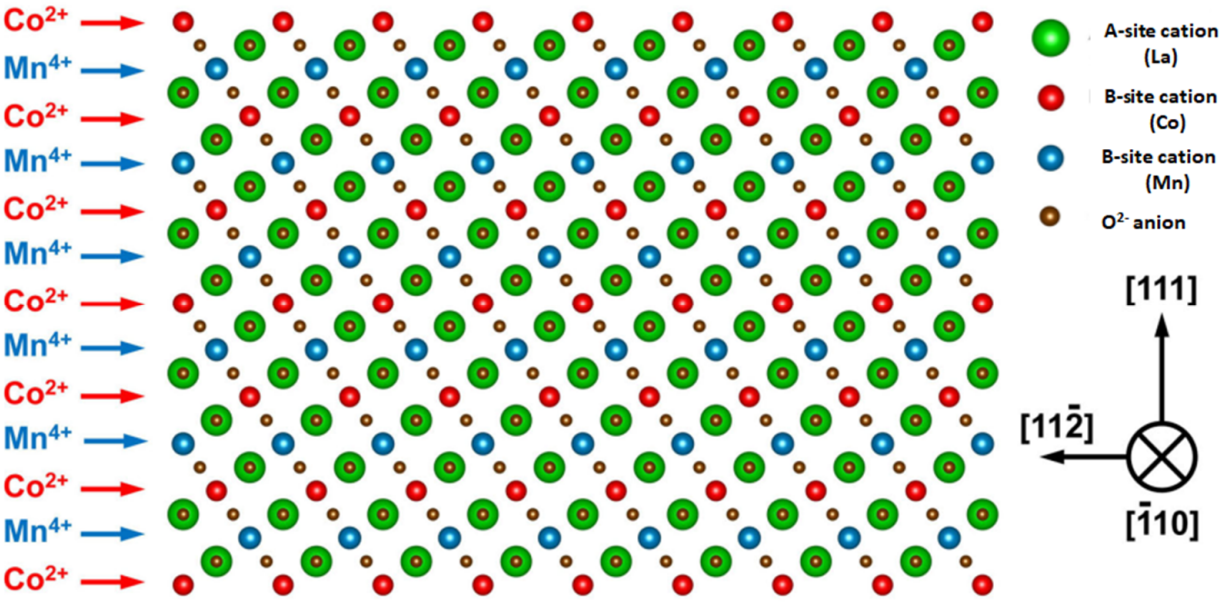


**Figure 2.** Lattice superstructure composed of $LaMnO_3$ and $LaCoO_3$ perovskite atomic planes formed along the [111]-direction in a fully ordered $La_2CoMnO_6$ double perovskite (Vesta, [18]).

In addition to the two mentioned fundamental driving forces determined by the choice of cation types, the B-site ordering can also be influenced by deposition conditions (growth temperature and growth rate), and for thin films, by the choice of substrate and thus, the epitaxial strain [5,8,26]. The choice of the A-site cation can also affect a DP material as the oxidation state of the A-site cation influences the average valence of the B/B′ cations. For an $A^{2+}$ cation (e.g., Ca, Sr, Ba), the average valence of the B cations is four and the ordering can theoretically be achieved for the following valence combinations: $B^{4+}/B'^{4+}$, $B^{3+}/B'^{5+}$, $B^{2+}/B'^{6+}$, and finally, $B^{1+}/B'^{7+}$. On the other hand, an $A^{3+}$ cation (La, Pr, Nd etc.) requires that BB′ cations have an average valence of 3+, making possible the following options: $B^{3+}/B'^{3+}$, $B^{2+}/B'^{4+}$, and $B^{1+}/B'^{5+}$ [8]. Which valence distribution finally occurs depends not only on the B-order but also on the choice of elements for the cations as each element can have its preferred individual valence state according to the applied growth conditions, e.g., oxygen partial pressure.

To quantify the B-site ordering, a long-range degree of ordering, $s = 2g_B - 1$, is introduced; here, $g_B$ denotes the occupation of correct lattice sites by the B and B′ cations [8]. The completely ordered DP possesses a value of s = 1, which means that all sites are fully occupied by the correct cations and the so-called anti-site disorder, AS = 0. A completely disordered DP will have a value of s = 0. In between these two extreme situations, DPs are considered to be partially ordered, with a degree of ordering at $0 < s < 1$. Deviations from the fully ordered phase, otherwise known as lattice misoccupations, occur in the form of point defects (PD) with an anti-site disorder, in which the B and B′ cations as

well as the antiphase boundaries (APB) are exchanged, separating two ordered domains with opposite B and B′ occupations. PDs and APBs have different effects on the cation ordering in a DP material. In particular, the point defects destroy the short-range B-site ordering, yielding an occupation error and reducing the s-value to some extent. In contrast, the APBs can cause a drastic reduction in the long-range B-site order, yielding very small s~0 values. In the literature, the intensity ratio of the Bragg structural XRD peak, with (hkl) = (111), and of the superstructure peak (1/2 1/2 1/2) is often used to estimate the order by means of the parameter S = I(½ ½ ½)/I(111). However, this estimation of the local B-site order should be treated with caution; despite a high degree of local B-site ordering, the superstructure peak can be totally extinguished due to the presence of the APB domains with opposite orientations lying antiparallel to the scattering vector, thus giving a small total **s-value**. In bulk DP materials, B-site ordering can also be quantified by the ratio $[I(½\ ½\ ½)/I(200)]_{obs.}/[I(111)/I(200)]_{theo.}$ [11]; however, this cannot be used for thin epitaxial films because not all reflexes can be simultaneously measured in an XRD pattern.

It is therefore essential, especially for thin film studies, to include additional measurements and experimental data to determine the B-site ordering. These can be magnetization data taken for magnetic DP materials as well as Raman spectra, which were found to be informative as ordered (O) and disordered (D) DP materials crystalized in different crystal structures. With regard to magnetism, in a fully ordered LCMO DP, the superexchange interaction between the $Co^{2+}$ and $Mn^{4+}$ ions according to the second Goodenough–Kanamori–Anderson rule [6,18,28] results in a maximum value of saturation magnetization $M_{theo}$ = 6 $\mu_B$/f.u. This value can be used to estimate the "magnetic" degree of order as $s_{mag} = M_{meas.}(T = 4.2\ K)/M_{theo}$. Moreover, the Curie temperature of an ordered DP was found to be significantly higher than that of the disordered variant, i.e., for LCMO $T_C$(O)~230 K >> $T_C$(D)~130 K [6,18,28]. Raman spectroscopy is a powerful nondestructive spectroscopic technique, which allows the direct structural characterization of a DP material [21–25]. By measuring polarization-dependent Raman spectra, one can distinguish between the disordered (orthorhombic, *Pbnm*) and ordered (monoclinic, $P2_1/n$) variants as these structures possess different Raman selection rules. In addition, according to Truong et al. [25], even the admixture of ordered and disordered phases can be detected by Raman spectroscopy. However, these macroscopic techniques do not address the degree of cation ordering directly; further assumptions and knowledge of magnetic interactions and the structural determination of the phonon spectra are still needed. Finally, a transmission electron microscope (TEM) utilized for chemical mapping by means of atomically resolved electron energy loss spectroscopy (EELS) can be used to directly visualize the local B-site ordering on the atomic scale. However, this is less informative than APBs.

## 3. Cation Ordering in Thin Films

Nevertheless, the growth of B-site cation-ordered correlated oxide thin films is known to be a challenging task. As already mentioned, it requires growth conditions—e.g., substrate temperature, growth rate, partial pressure of oxygen—to be compatible with those favoring the cation ordering. As mentioned above, the driving forces for cation ordering in bulk (single crystals) oxides are charge and size mismatches between the involved B-site cations; $Co^{2+}$ and $Mn^{4+}$ as well as the NaCl type of order seem to be favorable for compensation of both charge and size mismatches. Considering the formation free energy of a DP, $E = U - TS$ (U is the inner energy, T and S are temperature and entropy, respectively), the energy minimum for the ordered phase can be achieved only if the temperatures are high enough as the entropy term for the ordered (O) variant is smaller than that for the disordered (D) one: $S_O < S_D$. However, at high temperatures, the increased growth kinetics of a DP film would also increase the entropy, hence favoring the disordered state [8]. Thus, a compromise between the thermodynamics and kinetics has to be found in order to achieve the growth of cation-ordered DP films. It is worth noting that all possible deviations from the stoichiometry, e.g., A/B and B/B′ atomic ratios, and growth-induced

defects, e.g., oxygen vacancies and interstitial atoms, would favor the disordered phase by the entropy term. It seems reasonable to assume that the film growth conditions close to the equilibrium, i.e., high temperatures and low degree of supersaturation, together with a fine control of the chemical composition could be favorable for achieving the ordering.

Thin films of DP, including those of LCMO and LNMO, have been prepared by well-elaborated and widely used thin film vacuum deposition techniques, such as PLD, sputtering, and MBE. Particularly noteworthy is the fact that reports on PLD-grown DP films dominate the literature, whereas the MBE is much less presented. In general, the film growth within PLD and sputtering is usually considered a non-equilibrium and kinetically controlled process as the deposition species (atoms, clusters, molecules) possess high kinetic energy and are able to create defects in the growing film. However, although the MBE technique is free from the above-mentioned effects and provides near-to-equilibrium growth conditions, it also operates at low oxygen pressure, $pO_2$~$10^{-5}$ mbar [29]. This results in oxygen deficiency and weak saturation magnetization in the as-grown MBE-grown films; for example, the LNMO films show only $M_{sat}$~1.3 $\mu_B$/f.u. [29], which increases up to $M_{sat}$~3.5 $\mu_B$/f.u. after post-annealing, remaining significantly smaller than the theoretical value $M_{theo}$ = 5 $\mu_B$/f.u. for a fully ordered LNMO [23]. Comparing MBE with the PLD and sputtering, the two latter techniques offer higher oxygen pressure, $pO_2$~0.1 mbar [30] during deposition. However, the problem of oxygen deficiency and/or preparation-induced defects for PLD-grown films probably still exist in order to obtain strong magnetic properties; for example, in LCMO films [31] a post-annealing in 500 mbar of oxygen at 700 °C was shown to be a necessary condition. Several reports on the growth of LCMO [32] and LNMO [33] films by rf-sputtering under $pO_2$~0.1–0.5 mbar also pointed out the importance of post-annealing in the improvement of oxygen stoichiometry and magnetism in these films. Truong et al. [25] reported the influence of growth conditions (temperature/$pO_2$) on the Ni/Mn ordering, studied by Raman spectroscopy, in the PLD-grown LNMO(111)/STO(111)films. The long-range ordered (O) phase was grown at 800 °C/1 mbar, the disordered (D) phase at 500 °C/0.4 mbar, while the O + D admixture was at 800 °C/0.4 mbar. These results outline the importance of both high growth temperatures and high oxygen pressure to achieve the B-site ordering.

In contrast to the PVD routes, which operate far from equilibrium and at reduced oxygen pressure, chemical routes such as the metalorganic aerosol deposition (MAD) [34,35] as well as other solution-based techniques such as PAD [36] can provide growth conditions close to the equilibrium. Moreover, the MAD growth occurs at a very high partial oxygen pressure, $pO_2$~200 mbar, usually at ambient air or even in an oxygen-rich atmosphere. All this allows the oxidation of precursors and prevents oxygen deficiency in the grown films. With regard to the MAD growth, the process is based on the heterogeneous pyrolysis reaction of the aerosols of metalorganic precursor solutions on the surface of a heated substrate [34]. This results in an extremely high-density vapor/liquid phase of precursors and a diffusion-controlled growth rate of $v_g$~1–5 nm/min due to a high substrate temperature of $T_{sub}$~800–950 °C, which ensures a low supersaturation and generally preventing the fast heterogeneous nucleation of 3D clusters. One can compare the MAD growth conditions with those of a liquid phase epitaxy (LPE), yielding a homogeneous and defect-free growth of an oxide film according to the "step-flow" or layer-by-layer 2D growth mode. The advantage is a drastic decrease in the temperature-dependent supersaturation degree, $\alpha$, and a concomitant increase in the nucleation cluster size, $r_S$~$1/\alpha$ [37,38]. The large size of crystalline domains allows one to reduce the amount and the influence of point defects as well as the possible antiphase boundaries in the grown film. This seems to be important for the control of cation and anion stoichiometry during epitaxy, as we have demonstrated earlier, by the ability to grow the A-site ordered $La_{3/4}Ca_{1/4}MnO_3$ [39] films, in which the La/Ca order was shown to significantly increase the phase transition temperature. As a result, the MAD growth conditions allow one to obtain epitaxial oxide films and heterostructures, including double perovskites, with high crystalline quality, perfect surface morphology, and optimally high functional properties as was demonstrated earlier for

cuprates [40], manganites [39], ruthenates [41], titanites [34], nanocomposites [42], and superlattices [35].

As mentioned above, an important issue for epitaxial DP thin films is the lattice misfit stress. Usually, LCMO and LNMO DP films are grown by PLD and sputtering on single-crystalline functional oxide film substrates with a perovskite structure, e.g., STO, $LaAlO_3$ (LAO) and $(La_{0.3}Sr_{0.7})(Al_{0.65}Ta_{0.35})O_3$ (LSAT), with a lattice misfit, $\varepsilon = 100\% * (a_F - a_S)/a_F$ from −3% to +0.5% [30,43]. According to Kleibeuker et al. [31] the strongest magnetism with $M_S$(5 K)~6 $\mu_B$/f.u. and $T_C$~211 K was observed in LCMO film grown on the LSAT(111) substrate, actuating a small compressive in-plane stress. The films grown on STO (small tensile) and LAO (relaxed) substrates display significantly lower $M_S$(5 K)~3.5–4 $\mu_B$/f.u. and Curie temperatures, especially on the (100) substrates $T_C$ = 113 K (STO) and 125 K (LSAT), pointing out that these films are B-site disordered. However, no structural characterization of the B-site ordering was provided to compare with magnetic data. It is worth noting that in the case of the (100)-oriented substrates, the B-site ordering could be estimated only indirectly from the magnetization data [14] or Raman spectroscopy [22,24].

The LCMO films with a high degree of short-range Co/Mn ordering were grown by metalorganic aerosol deposition technique on sapphire [5] and STO(111) [6] substrates (see Figure 3). An atomic force microscopy (AFM) image demonstrates flat surface morphology with the estimated mean-square-roughness, RMS = 0.25 nm. The long-range ordering, quantified by a macroscopic XRD degree of ordering, **s** = I(½ ½ ½)/I(111) = 1.1 × $10^{-3}$, was, however, much smaller than the theoretical value, **s** = $10^{-2}$, calculated for a fully ordered LCMO, possibly indicating the presence of antiphase boundaries [6]. The local Co/Mn ordering, obtained by atomically resolved chemical mapping with EELS and shown in Figure 3, shows the neighboring (111) atomic planes occupied predominantly with Co and Mn ions; however, the full ordering cannot be detected. The valence states of the transition metal cations of $Mn^{4+}$ and $Co^{2+}$, experimentally determined by TEM and EELS measurements, point to a globally ferromagnetic ground state due to a $Co^{2+}$-O-$Mn^{4+}$ ferromagnetic super-exchange interaction. High Curie temperatures, $T_C$ = 226 and 228 K, and high saturation magnetization, $M_S$(4.2 K) = 5.8 and 5.9 $\mu_B$/f.u., were measured for LMCO(111)/STO(111) and LMCO(111)/$Al_2O_3$(0001) films [5,6]. They both indicate a high degree of short-range Co/Mn ordering, s = 0.97, 0.98, estimated as a ratio between the measured saturation magnetization and the maximal theoretical magnetization for the ordered LCMO $M_S$(theo.) = 6 $\mu_B$/f.c., assuming the ferromagnetically coupled spins of $Co^{2+}$ and $Mn^{4+}$ ions. Worthy of note is the fact that the disordered LCMO films possess much smaller values of $M_S$(4.2 K) = 3.5–4.5 $\mu_B$/f.u., as was shown for PLD-grown films earlier [24,30].

Comparing the MAD- and PLD-grown thin LCMO films on STO(111) substrates, one can see a clear improvement of ordering in the MAD-grown films. Particularly, in the PLD-grown films, a saturation magnetization of $M_S$(4.2 K)~4 $\mu_B$/f.c. indicates only a partial ordering with **s**~0.67 [31]. As mentioned in previous studies on PLD-grown LCMO films, non-equilibrium growth conditions result in oxygen vacancies, which are detrimental to B-site ordering [32]. Even by decreasing deposition temperature and similarly high $M_S$ in LCMO(111)/LSAT(111) grown by PLD [31], the short-range Co/Mn ordering registered by TEM–EELS imaging is far from being considered perfect. In addition, the EELS spectra taken with low energy resolution do not show fine features inherent in $Mn^{4+}$ and $Co^{2+}$ ions. It is worth noting that the Co/Mn ordering shown in Figure 3 for the LCMO(111)/STO(111) film grown by MAD, taken together with clearly defined $Co^{2+}$ and $Mn^{4+}$ oxidation states in the EELS spectra, allow us to conclude that close-to-equilibrium growth within MAD, accompanied by high oxygen partial pressure, are much more effective for cation ordering than a non-equilibrium growth within PLD and sputtering. Recently, Wang et al. [36] obtained the Co/Mn ordering in LCMO/STO(100)-grown film by using another near-equilibrium PAD technique. This nontraditional solution-based technique employs metal–polymer solutions as film precursors, which after spin coating onto a substrate and subsequent drying undergo a solid-state reaction at high temperatures

of ~900 °C and flow oxygen conditions. The order was confirmed by strong magnetism ($T_C$ = 230 K and $M_S$~6 $\mu_B$/f.u.) and local TEM–EELS maps, indicating an ordered Co/Mn occupancy of B-sites. Thus, recent PAD and MAD results strongly support the thesis that the near-equilibrium growth conditions, i.e., high temperatures of $T_{sub}$~900–950 °C and high $pO_2$~0.2–1 bar within chemical deposition routes promote the cation ordering. However, even within short-range ordered domains in the MAD-grown films, a complete macroscopic ordering over the whole film thickness is still a challenge due to the presence of defects, such as APBs [7] as well as twinning domains, with an orientation misfit of ~0.3° observed in LCMO(111)/$Al_2O_3$(0001) films [5]. In the latter case, the relaxation of the orientation misfit at the domain boundary by changing the (B,B')-O bond lengths results in Jahn–Teller distortions and the formation of $Mn^{3+}$ and $Co^{3+}$ ions.

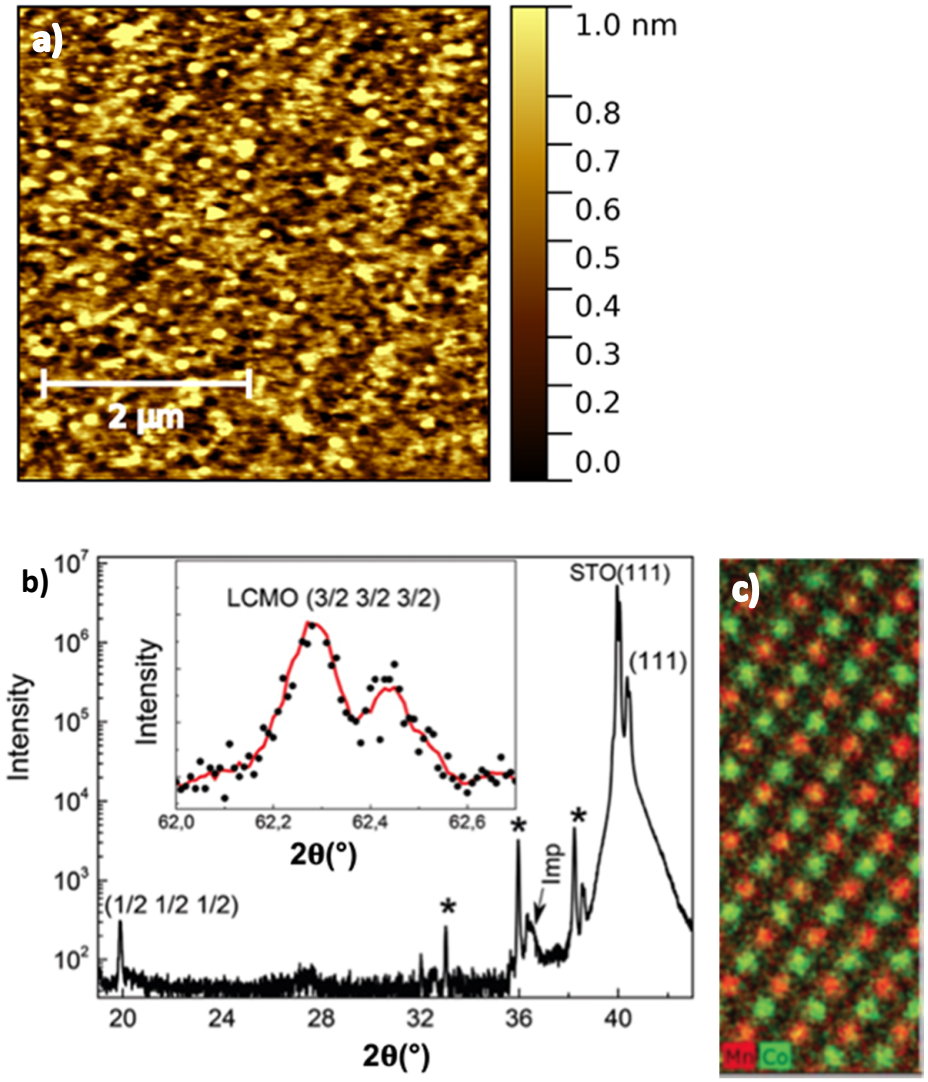


**Figure 3.** (**a**) AFM image of the surface morphology of a $La_2CoMnO_6$ (LCMO) film grown by MAD technique on STO(111) substrate; (**b**) XRD pattern of the LCMO(111) film shows superstructure peaks and (**c**) short-range Co/Mn ordering evidenced by TEM-EELS mapping with Mn(red) and Co(green) dots. (**b**,**c**) are reproduced from Ref. [6] with permission from the European Society for Photobiology, the European Photochemistry Association, and The Royal Society of Chemistry.

The DP films grown on (111)-oriented substrates like LCMO/STO(111) [5,6,31] are preferable for studies because both the short- and long-range B-site order can be compared from XRD, TEM–EELS, Raman, and magnetization data. The observed strong dependence of the magnetic properties of a DP material on the crystalline structure and on the B-

site ordering can also be interpreted within a magneto-elastic concept, quantified by the so-called spin–phonon coupling constant, λ, which can be directly determined from the temperature-dependent measurements of Raman spectroscopy [22,24]. The onset of ferromagnetic ordering at $T_C$ results in a distinct softening of the breathing phonon mode with $A_g$ symmetry, which reflects the increase of a bond length or volume in a ferromagnetic material; meanwhile, as an FM exchange interaction between $Co^{2+}$-$Mn^{4+}$ spins, described within the fundamental concept of an exchange hole [44], ions tend to move away from each other. The magnetization-induced change of position of the Raman mode, Δω(T), relative to the anharmonic contribution, $\omega_{anh}(T)$, is described [22] as follows:

$$\Delta\omega(T) = \omega(T) - \omega_{anh}(T) \approx -\lambda(S_i \cdot S_j) \approx -4\lambda * [M^2(T)/M^2(0)]$$

Thus, a spin–phonon interaction can be quantified by the spin–phonon coupling constant, λ, which describes the strength of the magneto-elastic coupling in a DP material and is important for magneto-dielectric applications. In Figure 4, we present the experimentally measured λ values in LCMO films grown on (111)-oriented substrates, actuating different signs and values of epitaxy stress [5]. One can see that the strongest spin-phonon coupling constant, λ = 2.1 $cm^{-1}$, was obtained for the highly ordered LCMO film (s = 0.98) grown on sapphire, which actuated a very small in-plane compressive stress. Moreover, a large lattice mismatch significantly reduced spin–phonon coupling down to λ∼1.5 $cm^{-1}$ for $LaAlO_3$(111) with compressive stress, and to λ∼1.4 $cm^{-1}$ for STO(111) with tensile stress. It is worth noting that PLD-grown LCMO films on STO(100) substrates show a value of $\lambda \approx 1$ $cm^{-1}$ [24].

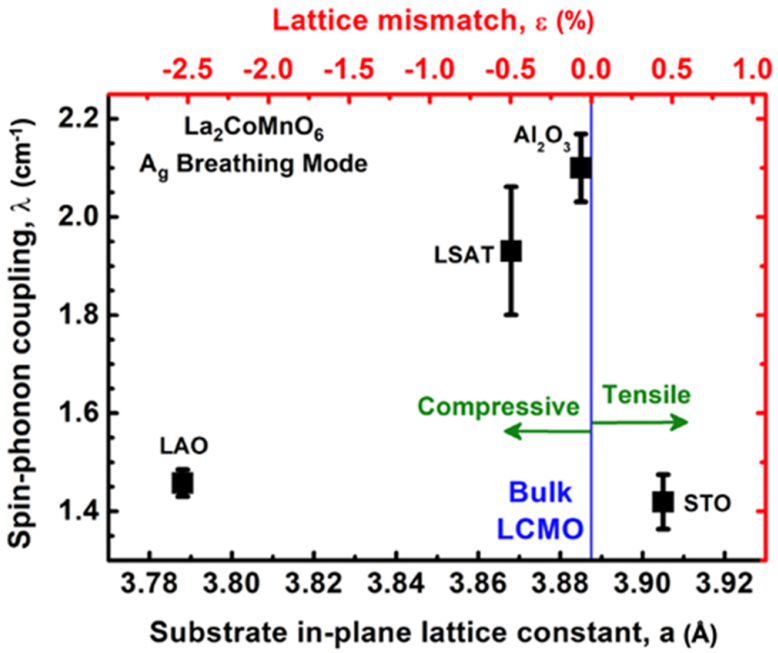


**Figure 4.** Spin-phonon coupling strength, $\lambda$, of the *B*-site ordered LCMO(111) thin films grown by MAD on different substrates, as a function of the in-plane lattice constant of the used substrates, $a_{Sub}$, or of the corresponding in-plane lattice mismatch, $\varepsilon = 100\% * (a_{Sub} - a_{LCMO})/a_{LCMO}$, with respect to the lattice constant of the bulk LCMO, $a_{LCMO}$ = 0.3887 nm. Adopted with permission from American Physical Society (Copyright 2018) ref [5].

## 4. Cation Ordering in Artificial Heterostructures

Based on the results presented in the previous section, we believe that the close-to-equilibrium chemical deposition techniques such as the PAD and MAD techniques, which enable a high degree of order in LCMO(111)/STO(111) films [5,6,36], can be viewed as promising routes for approaching the ultimate atomic-level control in artificial cation-

ordered lattices of correlated oxides. It is worth noting that the realization of ordering by growing the short-period superlattices (SLs) was considered to be extremely difficult within PLD [31]. During the peer review, we were aware of the fact that there was indeed an existing report on the PLD-grown B-site ordered DP as an SL that consists of single atomic layers of $[(SrRuO_3)_{1\ u.c.}/(SrFeO_3)_{1\ u.c.}]_{55}$ on STO(111), published by Chang et al. [45]. The long-range ordering at s = 0.5 and short-range "magnetic" degree of ordering of about 80% (after post-annealing) were obtained and confirmed by electron diffraction and TEM–EELS maps. In addition, the determined Curie temperature of the ordered $Sr_2FeRuO_6$ (SFRO) SL, $T_C$~400 K, is much larger than that of the corresponding disordered SFRO bulk material at $T_C$~60 K. Worthy of note is the fact that the lack of ordering in bulk SFRO was attributed to the insufficient valence-size mismatch between the $Ru^{5+}$ and $Fe^{3+}$ cations. Thus, these results can also be viewed as a successful demonstration of the realization of the B-site ordering in the artificial film structure, whereas the ordering was absent in the bulk SRFO.

In the next section, we address the recently published cation ordering in the MAD-grown $LaMnO_3/LaNiO_3$ (LMO/LNO) SLs [24] as well as the realization of B-site ordering in the layer-by-layer (LL) MAD-grown $LaMnO_3/LaCoO_3$ SLs. The SLs can be viewed as precursor heterostructures to "seed" the ordering as an emergent interfacial phase, e.g., $La_2NiMnO_6$ in LMO/LNO SLs [9], and then to enlarge the DP phase through the whole sample by decreasing the thickness of individual layers down to one perovskite u.c. To achieve this task, we further developed the in situ growth control by optical ellipsometry [34,35], allowing us to grow films in an LL mode, i.e., by sequential deposition of single atomic layers of $ABO_3/AB'O_3/ABO_3/\ \ldots$ .

### *4.1. B-Site Ordered Emergent Phase in $LaNiO_3$/$LaMnO_3$ Superlattices*

Our interest in the $LaNiO_3/LaMnO_3$ (LNO/LMO) SLs as "precursor" heterostructures to the growth of the DP $La_2MnNiO_6$ (LNMO) phase was motivated by high Curie temperatures of $T_C$~290 K and observations of the magnetodielectric effect in LNMO material [12,13]. We believe that the differences between the PLD and MAD-grown heterostructure samples become clear by considering the LNO/LMO SLs. From a crystallographic point of view (see Figure 2), the growth of these structures as a sequence of LMO/LNO atomic layers along the [111] crystallographic direction should result in an ordered $La_2MnNiO_6$ film, with structure and properties similar to those seen in the DP LNMO [13]. However, the DP LNMO phase has not been detected in the PVD grown SLs [46–51]. In contrast, the MAD-grown $[(LNO)_n/(LMO)_n]_m$ (with n = 1, 2, 5, 10, 20 u.c. and m = 100, 50, 20, 10, 5) SLs on STO(111) [9] clearly demonstrate the presence of an emergent LNMO phase at the interfaces for relatively thick layers, n = 10 and 5 u.c., followed by its dominance for short-period SLs with n = 1, 2. This is evidenced by both magnetic and Raman spectroscopy measurements, shown in Figures 5 and 6, respectively. Indeed, one can see in Figure 5 that 10/10 and 5/5 SLs reveal two ferromagnetic phases with high and low $T_C$ values associated with the interface and bulk-like LMO contributions, respectively [9]. For comparison, the M(T) curves of ferromagnetic single films of LMO(111)/STO(111) (a) and of the so called "state-of-the-art" (SoA) LNMO(111)/STO(111) prepared from one precursor solution (f) are also shown in Figure 5. It is worth noting that in the 20/20 SL, only magnetic contribution from the LMO layers can be resolved and 20 u.c. thick (~2.2 nm) LNO layers still preserve their natural metallic behavior (not shown). Accordingly, in Figure 6, the polarization-dependent Raman spectroscopy unambiguously evidences the breathing ($A_g$ @ 670 $cm^{-1}$) and mixed ($B_g$ @ 530 $cm^{-1}$) modes characteristic of the ordered DP LNMO [23] material with a monoclinic $P12_1/n1$ structure in all SLs under study. With the decreasing thickness of LMO and LNO layers, the intensity of Raman modes increases and their linewidth decreases, until finally, the spectra of 2/2 and 1/1 SLs do not differ from those measured in the SoA LNMO film.

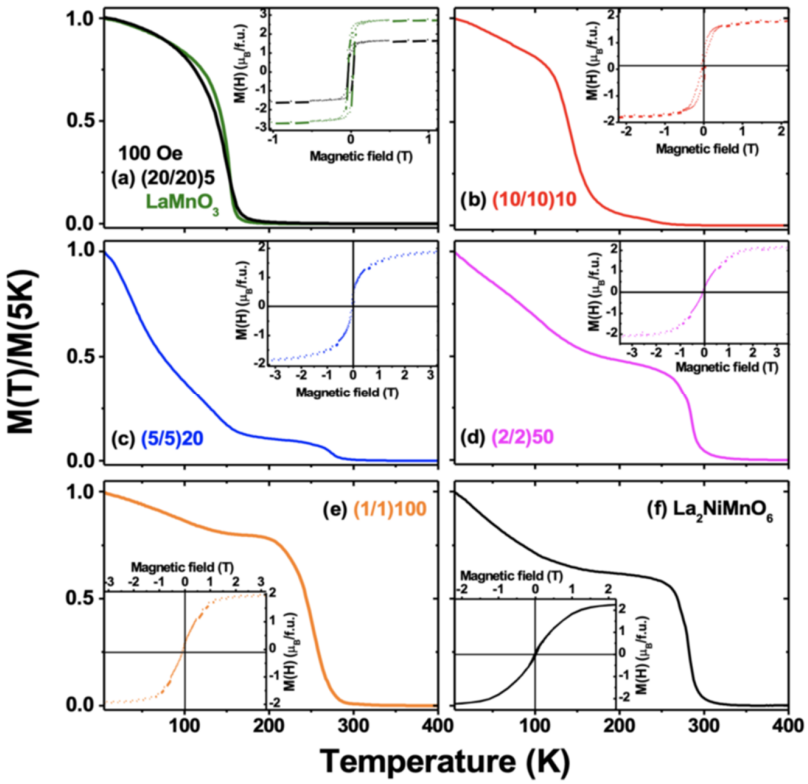


**Figure 5.** Temperature, M(T), and magnetic field, M(H), (inset at H = 100 Oe) dependences of magnetization (**a**) of the $LaMnO_3$ film (green) with thickness at $d_{LMO}$ = 16 nm, and of the nLMO/nLNO (n/n) SLs (20/20, black); (**b**) (10/10, red); (**c**) (5/5, blue); (**d**) (2/2, magenta); (**e**) (1/1, orange); and (**f**) (SoA, black) grown by MAD technique. Adopted with permission from American Physical Society (Copyright 2021) ref. [9].

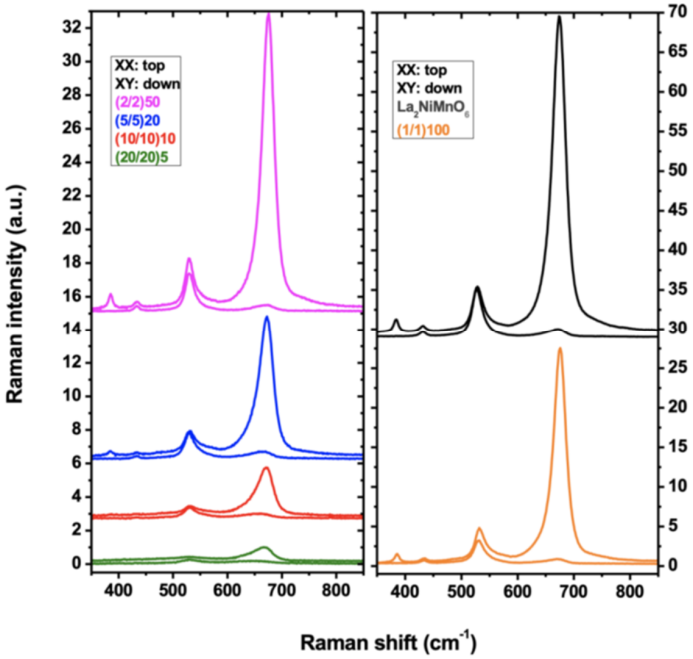


**Figure 6.** Polarized Raman spectra of nLNO/nLMO (n/n) SLs (20/20, olive), (10/10, red), (5/5, blue), (2/2, magenta), (1/1, orange), and of the LNMO film (black), measured in XX and XY polarization configurations. Adopted with permission from American Physical Society (Copyright 2021) ref. [9].

The formation of emergent the LNMO DP phase detected by magnetic and Raman measurements in LMO/LNO SLs means that $Ni^{2+}$ and $Mn^{4+}$ oxidation states are realized at the interfaces, yielding a ferromagnetic superexchange interaction and structural transformation into a monoclinic phase. In other words, a charge transfer (CT) reaction such as $Mn^{3+} + Ni^{3+} \rightarrow Mn^{4+} + Ni^{2+}$ should occur at the interface, with one $e_g$ electron from Mn being transferred to Ni. As we showed recently [35], the CT at $SrMnO_3$(top)/$LaMnO_3$(bottom) interfaces can be effectively detected by the in situ optical ellipsometry within MAD. Using the same approach, the growth and CT at the interfaces in 10/10, 5/5, and 2/2 LNO/LMO SLs was monitored in situ by measurements of the ellipsometric phase shift angle, Δ(t), as shown in Figure 7. One can see that within the first 2–3 u.c. from the interface, both LNO and LMO layers in 10/10 and 5/5 SLs display modified electronic properties. This indicates a CT from the LMO into the LNO layer underneath, governed by a larger electronegativity of Mn compared to Ni [46], as well as a chemical/structural roughening at the LNO(top)/LMO(bottom) interfaces, as reported previously [46,47]. In contrast, in the 2/2 SL with a layer thickness very close to the CT length of ~ 2–3 u.c., the LMO layers, which have already given the electrons to the LNO underneath, show almost constant electronic properties. Moreover, the growth of the LNO layer onto the electronically exhausted LMO without JT distortions also seems to be problem-free. Thus, considering magnetic, Raman, and ellipsometry measurements, we can conclude that charge transfer at the LNO/LMO interfaces, accompanied by their structural transformations, indeed drives the formation of emergent DP LNMO phase. For the short-period 2/2 and 1/1 SLs, the properties are very similar to those of SoA LNMO films [9].

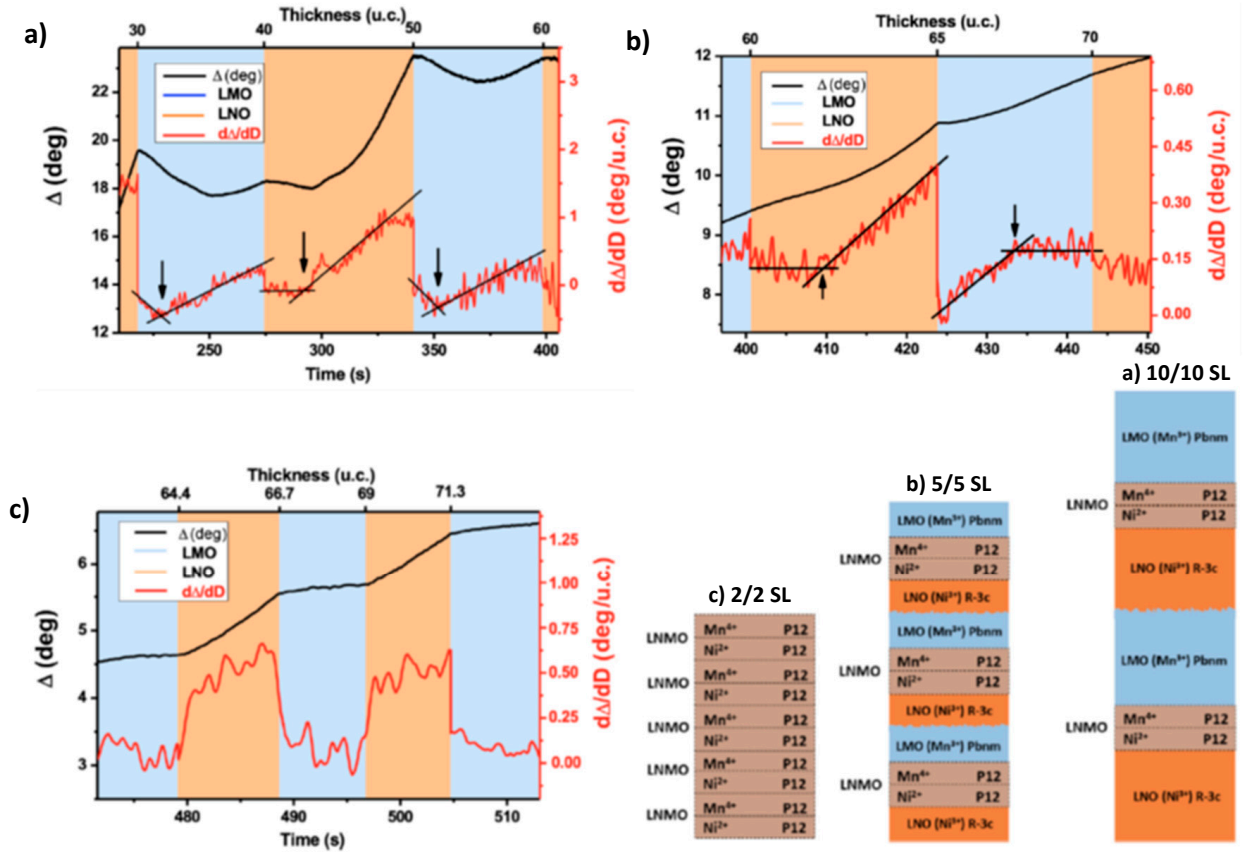


**Figure 7.** Ellipsometry diagrams of (**a**) 10/10, (**b**) 5/5, and (**c**) 2/2 SLs and the model of electronic/structural phase distribution in these SLs. Adopted with permission from American Physical Society (Copyright 2021) ref. [9].

### *4.2. Cation Ordering in the $La_2CoMnO_6$ Films Grown by LL-MAD*

To the best of our knowledge, no indications of the emergent DP phase in the $LaCoO_3/LaMnO_3$ (LCO/LMO) SLs were found in the literature [52–54]. We believe that the demonstrated cation-ordered $(LCO)_1/(LMO)_1$ SL below confirms the importance of the near-equilibrium MAD growth conditions for the LL growth of DP materials. However, the development of the MAD technology towards the LL growth mode makes sense if it can lead to better results than the conventional SoA growth. To prove this, we used the material system LCMO, in which a high degree of ordering was already obtained [5,6].

To grow the initial LL-grown LCO/LMO SL the $La(acac)_3Co(acac)_2$- and $La(acac)_3Mn(acac)_2$ precursor solutions were sprayed alternately (with pauses ~2 s between them and a precursor feeding rate ~1 µL/s) onto the heated substrate $T_{sub}$~950 °C. The solution volume necessary for the growth of 1 u.c. of the corresponding perovskite was determined separately in the previously grown single LCO and LMO films, $V_{LCO}$ = 3.82 µL/u.c. and $V_{LMO}$ = 3.8 µL/u.c., respectively. For the growth of the SoA LCMO film, the three precursors ($La(acac)_3$, $Co(acac)_2$, and $Mn(acac)_2$) were dissolved in one solution. Figure 8 shows the XRD results of the produced samples. The SoA film (blue) is considered a reference sample as it shows the expected c-lattice parameter $c_{SoA}$ = 0.387 nm and the superstructure peak at 2θ = 19.9° as an indication of a long-range B-site ordering. The evaluated ~88% degree of B-site ordering from the saturation magnetization $M_S$(5K) = 5.3 $\mu_B$/f.u. was lower than already reported [5,6] possibly since the growth parameters for this sample were not optimized.

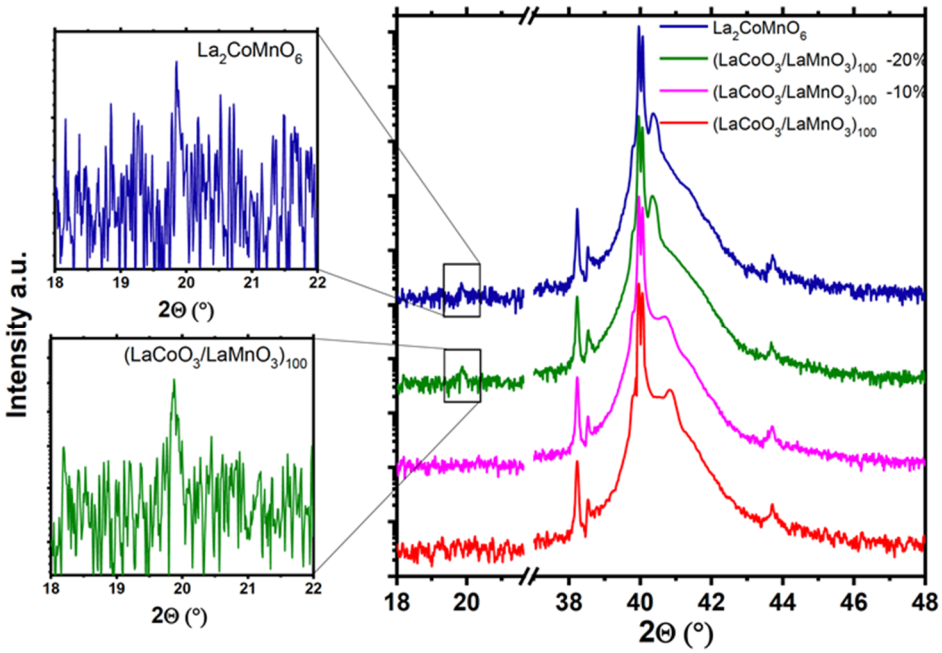


**Figure 8.** XRD measurements of LCMO SoA (blue), LCO/LMO SL: L1(red), L2 (magenta), and L3 (green).

Structural and magnetic characteristics of the initially LL-grown (L1) SL are shown in red in Figures 8 and 9, respectively. One can see a significantly smaller C-lattice constant, evaluated from the XRD pattern, $C_{L1}$ = 0.383 nm, and the reduced saturation magnetization of $M_S$(5K) = 4.7 $\mu_B$/f.u., which are both considerably smaller than those in the SoA film. Upon comparing the lattice constant of the L1 sample with the C-lattice parameters of single LMO and LCO films, i.e., $C_{LMO}$~0.390 nm and $C_{LCO}$ = 0.3762 nm [55,56], we suggest that the reduced c-lattice constant of the L1 SL compared to the SoA sample (c = 0.387 nm) indicates an increased amount of the LCO phase in the L1 SL. This should probably correlate with an increased Co/Mn > 1 stoichiometry ratio in the L1 film, i.e., the amount of the deposited LCO was too high. To check these hypotheses, the samples L2 and L3

were grown using an LCO deposition volume reduced by ~10% $V_{LCO}$ = 3.44 μL/u.c. (L2) and by ~20% $V_{LCO}$ = 3.06 μL/u.c. (L3); the volume of LMO was kept constant. The XRD and magnetization are shown in Figures 8 and 9 as magenta (L2) and green (L3) curves. One can see in Figure 8 that XRD patterns clearly follow the suggested trend: by reducing the volume of the deposited LCO solution, $V_{LCO}$, the position of the (111) peak in XRD patterns of L2 and L3 samples shifts systematically towards the position of the LCMO(111) peak in the SoA LCMO film. Moreover, the magnetization measurements in Figure 9 reveal a clear correlation with structural results: the closer the lattice constant of SL is to the lattice constant of LCMO, the higher the values obtained for $T_C$ and saturation magnetization $M_S$ are. Furthermore, the sample L2 shows only a modest increase of $C_{L2}$ = 0.3861 nm and $M_S$ = 4.9 $\mu_B$/f.u., but still no evidence for the (½ ½ ½)-superstructure peak. Apparently, the L3 sample reveals a remarkable improvement as not only the C-lattice constant $C_{L3}$ = 0.387 nm matches exactly the value of the SoA film, but also the magnetism with $M_S$ = 6 $\mu_B$/f.u. and $T_C$ = 225 K is optimized, even exceeding the values of the SoA sample and approaching the theoretical maximum for LCMO. It is worth noting that the L3 sample also possesses the lowest value of coercive field, $H_c$~6 kOe, which is close to the best values obtained for highly ordered LCMO films [6,31]. This indicates the largest size of the ferromagnetically ordered domains and small AFM contributions from the AS and APBs. The microstructure of the L3 sample was further visualized by the TEM and EELS measurements (see Figure 10). One can see a homogeneously grown and defect-free film with a thickness d~80 nm (Figure 10a), and a flat and atomically smooth interface between the film and substrate (Figure 10b). The local B-site ordering can be seen in the inset in Figure 10b along the [111] direction. The alternating cation planes filled mainly with Mn and Co atoms are colored in green and red, respectively. Nevertheless, one can see the variations of color intensities between the neighboring (111) atomic planes, indicating that the complete Co/Mn within this region ordering was not achieved.

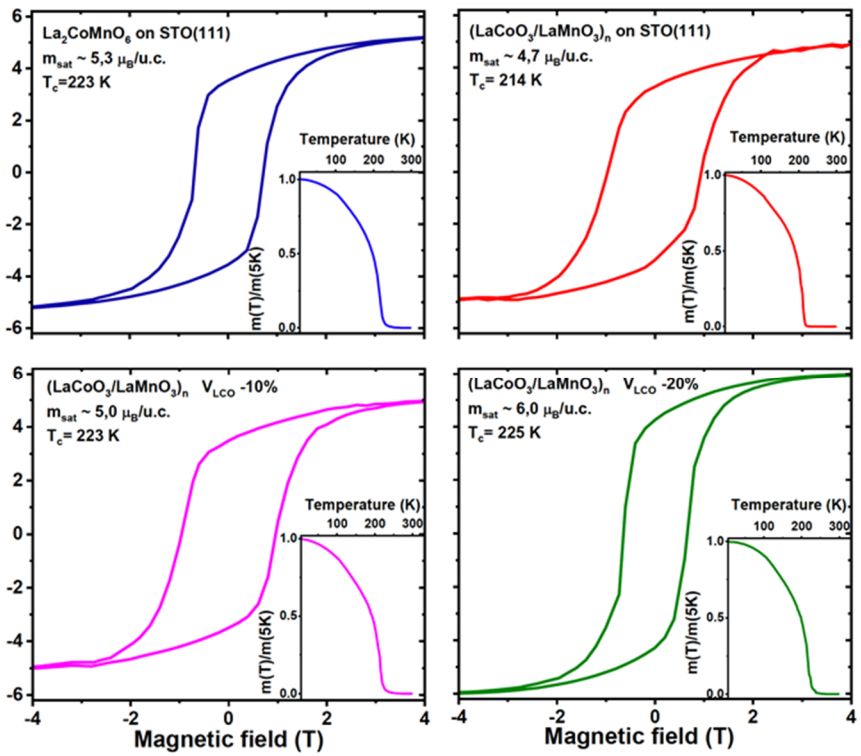


**Figure 9.** Magnetization m(B) at 5 K and m(T) at 1000 Oe (insert) of LCMO SoA (blue), LCO/LMO SL: L1(red), L2 (magenta), and L3 (green).

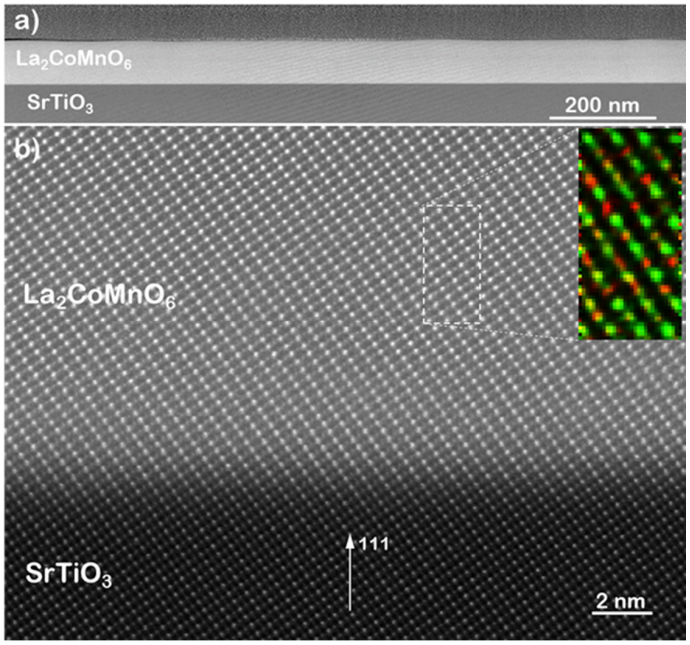


**Figure 10.** (**a**) High Angle Annular Dark Field (HAADF) image of the $La_2CoMnO_6$ L3 sample; (**b**) a high resolution HAADF image of LCMO/STO interface; the Mn (green)/Co(red) cation ordering in the dash-marked area is shown in the inset.

These results are further confirmed by the presence of the (1/2 1/2 1/2) peak in the L3 sample (see Figure 8), whose long-range ordering parameter is **s** = I(1/2 1/2 1/2)/I(111)~6 × $10^{-4}$, possesses a relative intensity that is much smaller than the theoretical value **s** = $10^{-2}$ for a complete Co/Mn ordering. In order to get a clear impression of the influence of the amount of the deposited $V_{LCO}$, further samples were produced with $V_{LCO}$ = 3.62 µL/u.c.; 3.30 µL/u.c.; 3.10 µL/u.c., and the results are summarized in Figure 11. One can see a definite correlation between the amount of $V_{LCO}$ and the structural and magnetic properties. In the range of 3.30 µL/u.c. < $V_{LCO}$ < 3.82 µL/u.c. there is an almost linear relationship between the lattice constant and the saturation magnetization. This knowledge allows us to create artificial $LCO_1/LMO_1$ heterostructures with structural and magnetic properties very similar to those of SoA LCMO film. However, the relations between the short- and long-range B-site ordering still remain unclear and require further studies.

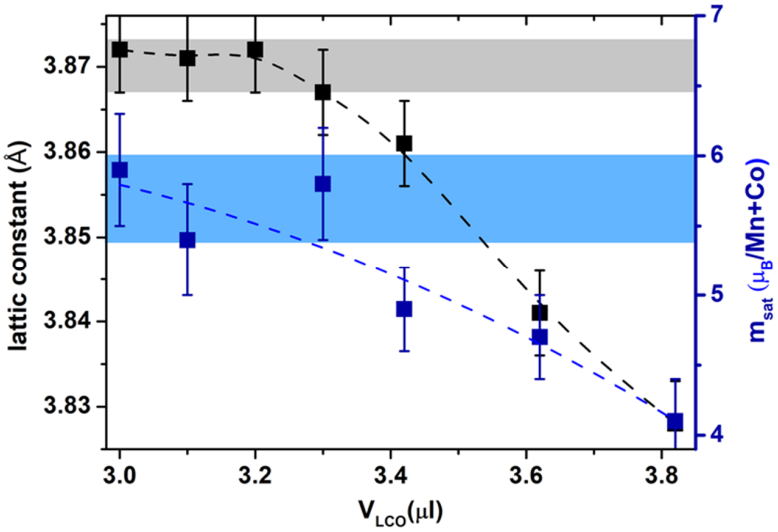


**Figure 11.** Impact of deposition volume $V_{LCO}$ on the lattice constant and the saturation magnetization of LCO/LMO SL grown by Layer-by-Layer mode.

## 5. Concluding Remarks

The B-site ordering in double perovskite bulk materials and in thin films, like the mostly studied systems of $La_2CoMnO_6$ and $La_2CoMnO_6$ is shown to be strongly affected by the mismatch in the B-site cation size and in the valence difference of the B-site cations. Probably, these two factors influence each other and, thus, enable to obtain a high degree of B-site ordering. A comparison between the physical (PLD, sputtering) and chemical (MAD and PAD) growth techniques shows that close to equilibrium growth conditions, easily achieved in the chemical solution-based techniques are favorable for the realization of B-site ordering in thin films. Nevertheless, the commonly used thin film growth methods do not allow a complete B-site order. This circumstance generates a chain of related questions about the ordering in thin films, which we will try to formulate below.

We believe that even with the assumption of the absence of deposition-induced defects and perfect growth conditions, interfaces/surface as unavoidable two-dimensional defects prevent the formation of a fully ordered DP thin film. The next question could be regarding the film thickness at which the influence of interfaces can be minimized. The thickness of the so-called "dead layer" with modified magnetic and structural properties of manganite ($La_{0.7}Sr_{0.3}MnO_3$) films 6–7 u.c.~2–3 nm [57] can perhaps be taken as a low boundary. This, however, needs to be directly proven by experiments. Another related question is whether a perfect ordering is necessary to obtain the property. Concerning ferromagnetism, the fully ordered DP films possess optimally high $T_C$ and large saturation magnetization, which manifest themselves by macroscopic magnetic measurements, usually at ~80% degree of the B-site ordering. However, the measurement accuracy of the saturation magnetization itself is ~10%, which makes this estimation not very reliable. On the other hand, since the crystal structures of the ordered and disordered phases are different, the admixture films (O + D) can be viewed as multiphase films, which can thus be inclined to degradation. The further question along this line is on how different techniques used to quantify the degree of ordering in thin films, i.e., XRD, Raman, magnetization, and TEM–EELS, can be related to each other? In other words, the degrees of long- and short-range ordering, obtained by XRD and TEM, respectively, do not necessarily correlate with each other. One needs techniques and simulation methods to evaluate the ordering on the mesosocopic scale, comparable with the film thickness, d~20–50 nm. This gap definitely exists as TEM–EELS mapping provides reliable images on a very short (atomic) scale. We believe that an interesting attempt to fill this gap was reported by Spurgeon et al. [29], as they succeeded in combining the ordering, viewed by TEM–EELS, at the atomic scale of 10–20 nm.

The superlattice approach to the B-site ordering within MAD, e.g., growth of LNO/LMO SLs, was shown to result in an emergent double perovskite phase at the LMO/LNO interfaces. This points out the importance of charge transfer at the interface, likely driven by the differences in the electronegativity between Ni and Mn cations in the realization of ordering. Moreover, the obtained emergent double perovskite LNMO phase in the LMO/SMO SLs is essentially two-dimensional, and likely possesses some unusual magneto-elastic properties deserving further study. Further promising avenues of research would be to apply the SL approach for the growth of DP materials, which do not show B-site ordering in bulk form. We have obtained preliminary results on that problem by comparing the SL and SoA MAD growth of $Sr_2RuTiO_6$ DP, which did not show ordering in bulk [58]. Surprisingly, one can see both long- (XRD) and short-range (TEM–EELS) ordering, driven by a charge disproportionation $Ru^{4+\delta}/Ti^{4-\delta}$ in the SoA film, whereas the $(SrRuO_3)_1/(SrTiO_3)_1$ SL does not show them. In order to promote the charge transfer and the resulting $Ru^{5+}/Ti^{3+}$ ordering, one most likely has to further tune the processing conditions such as oxygen pressure, deposition time, temperature, which in this case were not optimized for $Sr_2RuTiO_6$ DP.

Finally, the presented Layer-by-Layer growth route shows an opportunity to further tune the degree of B-place order by a controlled "layered" stoichiometry, i.e., by the LMO/LCO precursor ratio. Results show that the alternating deposition of the ABO/AB'O atomic layers, with pauses between the LCO and LMO pulses that allow atoms to completely fill the terraces, is promising and likely to suppress the formation of point defects

as well as antiphase boundaries. Further research is necessary to optimize the LL growth and stoichiometry control as there were still observed discrepancies between the short-and long-range B-site ordering in the LL-grown LCMO double perovskite films. Particularly, TEM and EELS measurements as well as magnetization (Ms = 6 $\mu_B$/f.c., $H_c$ = 6 kOe) confirm the high degree of short-range order and give no evidence of APB. However, this does not fit the degree of long-range ordering, quantified by the intensity of the (1/2 1/2 1/2) peak in XRD patterns. It is likely that the latter cannot be viewed as a reliable criterion and thus deserves further clarification.

**Funding:** This research was funded by DFG via Project Nos. MO-2255-4 and RO-5387/3-1, and the European Regional Development Fund and the State of Brandenburg for the Themis Z TEM (part of the Potsdam Imaging and Spectral Analysis Facility (PISA)).

**Acknowledgments:** This work was financially supported by the DFG via Project Nos. MO-2255-4 and RO-5387/3-1. V.R. acknowledges the European Regional Development Fund and the State of Brandenburg for the Themis Z TEM (part of the Potsdam Imaging and Spectral Analysis Facility (PISA)).

**Conflicts of Interest:** The authors declare no conflict of interest.

## References

1. Jonker, G.; Van Santen, J.; Jonker, G.; Van Santen, J. Ferromagnetic compounds of manganese with perovskite structure. *Physica* **1950**, *16*, 337–349. [CrossRef]
2. von Helmolt, R.; Wecker, J.; Holzapfel, B.; Schultz, L.; Samwer, K. Giant negative magnetoresistance in perovskitelike $La_{23}/Ba_{1/3}MnO_x$ ferromagnetic films. *Phys. Rev. Lett.* **1993**, *71*, 2331–2333. [CrossRef]
3. Bussmann-Holder, A.; Keller, H.H. *High Tc Superconductors and Related Transition Metal Oxides*, 1st ed.; Springer: Berlin, Germany, 2007; pp. 17–28.
4. Bednorz, J.G.; Muller, K.A. Possible high Tc superconductivity in the BaLaCuO system. *Z. Für. Phys. B Condens. Matter* **1986**, *64*, 189–193. [CrossRef]
5. Meyer, C.; Roddatis, V.; Ksoll, P.; Damaschke, B.; Moshnyaga, V. Structure, magnetism, and spin-phonon coupling in heteroepitaxial La2CoMnO$_6$/$Al_2O_3$(0001) films. *Phys. Rev. B* **2018**, *98*, 134433. [CrossRef]
6. Egoavil, R.; Hühn, S.; Jungbauer, M.; Gauquelin, N.; Béché, A.; Van Tendeloo, G.; Verbeeck, J.; Moshnyaga, V. Phase problem in the B-site ordering of $La_2CoMnO_6$: Impact on structure and magnetism. *Nanoscale* **2015**, *7*, 9835–9843. [CrossRef]
7. King, G.; Woodwaerd, P. Cation ordering in Perovskites. *J. Mater. Chem.* **2010**, *20*, 5785–5796. [CrossRef]
8. Vasala, S.; Karppinen, M. A2B'B"O6 Perovskites: A Review. *Prog. Solid State Chem.* **2015**, *43*, 1–36. [CrossRef]
9. Ksoll, P.; Mandal, R.; Meyer, C.; Schüler, L.; Roddatis, V.; Moshnyaga, V. Emergent double perovskite phase at $LaMnO_3/LaNiO_3$ interfaces: Coupled charge transfer and structural reconstruction. *Phys. Rev. B* **2021**, *103*, 195120. [CrossRef]
10. Serrate, D.; De Teresa, J.M.; Ibarra, M.R. Double perovskites with ferromagnetism above room temperature. *J. Phys. Condens. Matter* **2006**, *19*, 023201. [CrossRef]
11. Peters, J.J.P.; Sanchez, A.M.; Walker, D.; Whatmore, R.; Beanland, R. Quantitative High-Dynamic-Range Electron Diffraction of Polar Nanodomains in $Pb_2$ $ScTaO_6$. *Adv. Mater.* **2019**, *31*, e1806498. [CrossRef]
12. Rogado, N.S.; Li, J.; Sleight, A.W.; Subramanian, M.A. Magnetocapacitance and Magnetoresistance Near Room Temperature in a Ferromagnetic Semiconductor: $La_2NiMnO_6$. *Adv. Mater.* **2005**, *17*, 2225–2227. [CrossRef]
13. Choudhury, D.; Mandal, P.; Mathieu, R.; Hazarika, A.; Rajan, S.; Sundaresan, A.; Waghmare, U.V.; Knut, R.; Karis, O.; Nordblad, P.; et al. Near-room-temperature colossal magneto-dielectricity and multi-glass properties in partially disordered $La_2NiMnO_6$. *Phys. Rev. Lett* **2012**, *108*, 127201. [CrossRef]
14. Singh, M.P.; Truong, K.D.; Fournier, P. Magnetodielectric effect in double perovskite $La_2CoMnO_6$ thin films. *Appl. Phys. Lett.* **2007**, *91*, 042504. [CrossRef]
15. Yin, W.-J.; Weng, B.; Ge, J.; Sun, D.Q.; Li, Z.; Yan, Y. Oxide perovskites, double perovskites and derivatives for electrocatalysis, photocatalysis, and photovoltaics. *Energy Environ. Sci.* **2019**, *12*, 442–462. [CrossRef]
16. Ning, W.; Wang, F.; Wu, B.; Lu, J.; Yan, Z.; Liu, X.; Tao, Y.; Liu, J.-M.; Huang, W.; Fahlman, M.; et al. Long Electron-Hole Diffusion Length in High-Quality Lead-Free Double Perovskite Films. *Adv. Mater.* **2018**, *30*, e1706246. [CrossRef]
17. Ke, J.C.R.; Lewis, D.J.; Walton, A.S.; Spencer, B.F.; O'Brien, P.; Thomas, A.G.; Flavell, W.R. Abient-air-stable inorganic $Cs_2SnI_6$ double perovskite thin films via aerosol-assisted chemical vapour deposition. *J. Mater. Chem. A* **2018**, *6*, 11205–11214. [CrossRef]
18. Momma, K.; Izumi, F. VESTA 3 for three-domensional visualization of crystal, volumetric and morphology data. *J. Appl. Crystallogr.* **2011**, *44*, 1272–1276. [CrossRef]
19. Bhattacharya, A.; May, S.J. Magnetic Oxide Heterostructures. *Annu. Rev. Mater. Res.* **2014**, *44*, 65–90. [CrossRef]
20. Goldschmidt, V.M. Die Gesetze der Krystallochemie. *Naturwissenschaften* **1926**, *14*, 477–485. [CrossRef]

21. Iliev, M.N.; Abrashev, M.V.; Litvinchuk, A.P.; Hadjiev, V.G.; Guo, H.; Gupta, A. Raman Spectroscopy of Ordered Double Perovskite $La_2NiMnO_6$ Thin Films. *Phys. Rev. B* **2007**, *75*, 104118. [CrossRef]
22. Iliev, M.N.; Guo, H.; Gupta, A. Raman spectroscopy evidence of strong spin-phonon coupling in epitaxial thin films of the double perovskite $La_2NiMnO_6$. *Appl. Phys. Lett.* **2007**, *90*, 151914. [CrossRef]
23. Iliev, M.N.; Gospodinov, M.M.; Singh, M.P.; Meen, J.; Truong, K.D.; Fournier, P.; Jandl, S. Growth, magnetic properties, and Raman scattering of $La_2NiMnO_6$ single crystals. *J. Appl. Phys.* **2009**, *106*, 023515. [CrossRef]
24. Truong, K.D.; Laverdière, J.; Singh, M.P.; Jandl, S.; Fournier, P. Impact of Co/Mn cation ordering on phonon anomalies in $La_2CoMnO_6$ double perovsikter: Raman spectroscopy. *Phys. Rev. B* **2007**, *76*, 132413. [CrossRef]
25. Truong, K.D.J.; Singh, M.P.; Jandl, S. Fournier, Influence of Ni/Mn cation order on the spin-phonon coupling in multifunctional $La_2NiMnO_6$ epitaxial films by polarized Raman spectroscopy. *Phys. Rev. B* **2009**, *80*, 134424. [CrossRef]
26. Takahashi, R.; Ohkubo, I.; Yamauchi, K.; Kitamura, M.; Sakurai, Y.; Oshima, M.; Oguchi, T.; Cho, Y.; Lippmaa, M. A-site-driven ferroelectricity in strained ferromagnetic $La_2NiMnO_6$ thin films. *Phys. Rev. B* **2015**, *91*, 134107. [CrossRef]
27. Shannon, R.D.; Prewitt, G.R. Effective Ionic Radii in Oxides and Fluorides. *Acta Cryst.* **1968**, *B25*, 925–946. [CrossRef]
28. Dass, R.I.; Goodenough, J.B. Multiple magnetic phase of $La_2CoMnO_{6-\delta}$ ($0 \leq \delta \leq 0.05$). *Phys. Rev. B* **2003**, *67*, 014401. [CrossRef]
29. Spurgeon, S.; Du, Y.; Droubay, T.; Devaraj, A.; Sang, X.; Longo, P.; Yan, P.; Kotula, P.G.; Shutthanandan, V.; Bowden, M.E.; et al. Competing Pathways for Nucleation of the Double Perovskite Structure in the Epitaxial Synthesis of $La_2MnNiO_6$. *Chem. Mater.* **2016**, *28*, 3814–3822. [CrossRef]
30. Guo, H.Z.; Gupta, A.; Zhang, J.; Varela, M.; Pennycook, S.J. Effect of oxygen concentration on the magnetic properties of $La_2CoMnO_6$ thin films. *Appl. Phys. Lett.* **2007**, *91*, 202509. [CrossRef]
31. Kleibeuker, J.E.; Choi, E.-M.; Jones, E.D.; Yu, T.-M.; Sala, B.; MacLaren, B.A.; Kepaptsoglou, D.; Hernandez-Maldonado, D.; Ramasse, Q.M.; Jones, L.; et al. Route to achieving perfect B-site ordering in double perovskite thin films. *NPG Asia Mater.* **2017**, *9*, e406. [CrossRef]
32. Galceran, R.; Frontera, C.; Balcells, L.; Cisneros-Fernández, J.; López-Mir, L.; Roqueta, J.; Santiso, J.; Bagués, N.; Bozzo, B.; Pomar, A.; et al. Engineering the microstructure and magnetism of $La_2CoMnO_{6-\delta}$ thin films by tailoring oxygen stoichiometry. *Appl. Phys. Lett.* **2014**, *105*, 242401. [CrossRef]
33. Bernal-Salamanca, M.; Konstantinović, Z.; Balcells, L.; Pannunzio-Miner, E.; Sandiumenge, F.; Lopez-Mir, L.; Bozzo, B.; Herrero-Martín, J.; Pomar, A.; Frontera, C.; et al. Nonstoichiometry Driven Ferromagnetism in Double Perovskite $La_2Ni_{1-x}Mn_{1+x}O_6$ Insulating Thin Films. *Cryst. Growth Des.* **2019**, *19*, 2765–2771. [CrossRef]
34. Jungbauer, M.; Hühn, S.; Egoavil, R.; Tan, H.; Verbeeck, J.; Van Tendeloo, G.; Moshnyaga, V. Atomic Layer Epitaxy of Ruddlesden-Popper SrO($SrTiO_3$)n Films by Means of Metalorganic Aerosol Deposition. *Appl. Phys. Lett.* **2014**, *105*, 251603. [CrossRef]
35. Keunecke, M.; Lyzwa, F.; Schwarzbach, D.; Roddatis, V.; Gauquelin, N.; Müller-Caspary, K.; Verbeeck, J.; Callori, S.J.; Klose, F.; Jungbauer, M.; et al. High-TC Interfacial Ferromagnetism in $SrMnO_3/LaMnO_3$ Superlattices. *Adv. Funct. Mater.* **2020**, *30*, 1808270. [CrossRef]
36. Wang, H.; Gazquez, J.; Frontera, C.; Chisholm, M.F.; Pomar, A.; Martinez, B.; Mestres, N. Spontaneous cationic ordering in chemical-solution-grown $La_2CoMnO_6$ double perovskite thin films. *NPG Asia Mater.* **2019**, *11*, 44. [CrossRef]
37. Nishinaga, T.; Scheel, H.J. Crystal growth aspect of high-Tc superconductors. In *Advances in Superconductivity VIII*; Hayakawa, H., Enomoto, Y., Eds.; Springer: Tokyo, Japan, 1996; pp. 33–38.
38. De Yoreo, J.J.; Vekilov, P.G. 3. Principles of Crystal Nucleation and Growth. *Biomineralization* **2003**, *54*, 57–94. [CrossRef]
39. Moshnyaga, V.; Sudheendra, L.; Lebedev, O.I.; Köster, S.A.; Gehrke, K.; Shapoval, O.; Belenchuk, A.; Damaschke, B.; Van Tendeloo, G.; Samwer, K. A-Site Ordering versus Electronic Inhomogeneity in Colossally Magnetoresistive Manganite Films. *Phys. Rev. Lett.* **2006**, *97*, 107205. [CrossRef]
40. Khoroshun, I.V.; Karyaev, E.V.; Moshnyaga, V.T.; Kiosse, G.A.; Krachun, M.A.; Zakosarenko, V.M.; Davydov, V.Y. Characteristics of epitaxial Y-Ba-Cu-O thin films grown by aerosol MOCVD technique. *Supercond. Sci. Technol.* **1990**, *3*, 493–496. [CrossRef]
41. Schneider, M.; Geiger, D.; Esser, S.; Pracht, U.S.; Stingl, C.; Tokiwa, Y.; Moshnyaga, V.; Sheikin, I.; Mravlje, J.; Schneider, M.; et al. Low-Energy electronic properties of clean $CaRuO_3$: Elusive landau quasiparticles. *Phys. Rev. Lett.* **2014**, *112*, 206403. [CrossRef]
42. Moshnyaga, V.; Damaschke, B.; Shapoval, O.; Belenchuk, A.; Faupel, J.; Lebedev, O.I.; Verbeeck, J.; van Tendeloo, G.; Mücksch, M.; Tsurkan, V.; et al. Structural phase transition at the percolation threshold in epitaxial $(La_{0.7}Ca_{0.3}MnO_3)_{1-x}$:$(MgO)_x$ nanocomposite films. *Nat. Mater.* **2003**, *2*, 247–252. [CrossRef] [PubMed]
43. Galceran, R.; López-Mir, L.; Bozzo, B.; Cisneros-Fernández, J.; Santiso, J.; Balcells, L.; Frontera, C.; Martínez, B. Strain-induced perpendicular magnetic anisotropy in $La_2CoMnO_6-\varepsilon$ thin films and its dependence on film thickness. *Phys. Rev. B* **2016**, *93*, 144417. [CrossRef]
44. Ashcroft, N.W.; Mermin, N.D. *Solid State Physics*, 4th ed.; Oldenbourg Verlag: Oldenburg, Germany, 2012.
45. Chang, J.; Lee, K.; Jung, M.H.; Kwon, J.-H.; Kim, M.; Kim, S.-K. Emergence of Room-Temperature Magnetic Ordering in Artificially Fabricated Ordered-Double-Perovskite $Sr_2FeRuO_6$. *Chem. Mater.* **2011**, *23*, 2693–2696. [CrossRef]
46. Gibert, M.; Viret, M.; Torres-Pardo, A.; Piamonteze, C.; Zubko, P.; Jaouen, N.; Tonnerre, J.-M.; Mougin, A.; Fowlie, J.; Catalano, S.; et al. Interfacial Control of Magnetic Properties at $LaMnO_3/LaNiO_3$ Interfaces. *Nano Lett.* **2015**, *15*, 7355–7361. [CrossRef] [PubMed]
47. Gibert, M.; Viret, M.; Zubko, P.; Jaouen, N.; Tonnerre, J.-M.; Torres-Pardo, A.; Catalano, S.; Gloter, A.; Stephan, O.; Triscone, J.-M. Interlayer coupling through a dimensionality-induced magnetic state. *Nat. Commun.* **2016**, *7*, 11227. [CrossRef]

48. Gibert, M.; Zubko, P.; Scherwitzl, R.; Iñiguez, J.; Triscone, J.-M. Exchange bias in $LaNiO_3$–$LaMnO_3$ superlattices. *Nat. Mater.* **2012**, *11*, 195–198. [CrossRef] [PubMed]
49. Dong, S.; Dagotoo, E. Quantum Confinement Induced Magnetism in $LaNiO_3$-$LaMnO_3$ Superlattices. *Phys. Rev. B* **2013**, *87*, 195116. [CrossRef]
50. Hoffman, J.; Tung, I.C.; Nelson-Cheeseman, B.B.; Liu, M.; Freeland, J.W.; Bhattacharya, A. Charge Transfer and Interfacial Magnetism in $(LaNiO_3)n/(LaMnO_3)n$ Superlattices. *Phys. Rev. B* **2013**, *88*, 144411. [CrossRef]
51. Piamonteze, C.; Gibert, M.; Heidler, J.; Dreiser, J.; Rusponi, S.; Brune, H.; Triscone, J.-M.; Nolting, F.; Staub, U. Interfacial properties of $LaMnO_3/LaNiO_3$ superlattices grown along (001) and (111) orientations. *Phys. Rev. B* **2015**, *92*, 014426. [CrossRef]
52. Zhang, J.; Zhang, H.; Zhang, X.; Guan, X.; Shen, X.; Hong, D.; Zhang, H.; Liu, B.-G.; Yu, R.; Shen, B.; et al. Antiferromagnetic interlayer coupling and thus induced distinct spin texture for the $[LaMnO_3/LaCoO_3]$ 5 superlattices. *Nanoscale* **2017**, *9*, 3476–3484. [CrossRef]
53. Wu, L.; Chen, M.; Li, C.; Zhou, J.; Shen, L.; Wang, Y.; Zhong, Z.; Feng, M.; Zhang, Y.; Han, K.; et al. Ferromagnetism and matrix-dependent charge transfer in strained $LaMnO_3$–$LaCoO_3$ superlattices. *Mater. Res. Lett.* **2018**, *6*, 501–507. [CrossRef]
54. Guan, X.; Shen, X.; Zhang, J.; Wang, W.; Zhang, J.; Wang, H.; Wang, W.; Yao, Y.; Li, J.; Gu, G.; et al. Tuning ganetism and crystal orientations by octahedral coupling in $LaCoO_3/LaMnO_3$ thin film. *Phys. Rev. B* **2019**, *100*, 014427. [CrossRef]
55. Petrov, A.N.; Kononchuk, O.F.; Andreev, A.V.; Cherepanov, V.A.; Kofstad, P. Crystal structure, electrical and magnetic properties of $La_{1-x}Sr_xCoO_{3-y}$. *Solid State Ion.* **1995**, *80*, 189–199. [CrossRef]
56. Thornton, G.; Tofield, B.; Hewat, A. A neutron diffraction study of $LaCoO_3$ in the temperature range 4.2 <T <1248 K. *J. Solid State Chem.* **1986**, *61*, 301–307. [CrossRef]
57. Merten, S.; Bruchmann-Bamberg, V.; Damaschke, B.; Samwer, K.; Moshnyaga, V. Jahn-Teller reconstructed surface of the doped manganites shown by means of surface-enhanced Raman spectroscopy. *Phys. Rev. Mater.* **2019**, *3*, 060401. [CrossRef]
58. Pillai, S.S.; Santhosh, P.N.; Thomas, P.J.; Tuna, F.; Suresh, K.G. Structural, transport and magnetic properties of $Sr_2RuTiO_6$. *Sol. St. Comm.* **2010**, *150*, 1450–1452. [CrossRef]